Journal of Materials Chemistry

Cite this: J. Mater. Chem., 2012, 22, 5006

www.rsc.org/materials

PAPER

Synthesis of porous hollow Fe_3O_4 beads and their applications in lithium ion batteries†

Yu Chen,[a] Hui Xia,[b] Li Lu[b] and Junmin Xue*[a]

Received 25th October 2011, Accepted 5th January 2012
DOI: 10.1039/c2jm15440d

Porous hollow Fe_3O_4 beads constructed with rod-shaped Fe_3O_4 nanoparticles were synthesized *via* a facile solvothermal route. The formation mechanism of the obtained Fe_3O_4 beads was proposed on the basis of oriented assembly and Ostwald ripening. The as-prepared Fe_3O_4 beads had promising applications as lithium ion battery anodes, which showed a reversible specific capacity of 500 mAh g^{-1} after 50 cycles at 100 mA g^{-1}. After being decorated with a carbon coating layer, the Fe_3O_4/C composite beads showed an enhanced capacity of 700 mAh g^{-1} after 50 cycles at 100 mA g^{-1}. Such a satisfactory electrochemical performance was due to several factors of the Fe_3O_4/C composite beads including high theoretical capacity of Fe_3O_4, nanosized active Fe_3O_4 particles, hollow porous structure that mitigated the volume change problem, and carbon coating layer that enhanced both the electronic conductivity and structure integrity.

Introduction

Lithium ion batteries (LIBs) have attracted much attention in both scientific and industrial fields due to their higher energy density compared with other rechargeable battery technologies, making them an attractive choice for portable electronic devices.[1–3] In order to meet the requirements of new emerging technologies, the next generation of LIBs are expected to have superior performance in terms of capacity, cycling stability, and rate capability.[4] This goal significantly relies on developing a new generation of anode materials, which plays a crucial role in LIBs' performance.

During the past several years, many new anode materials have been proposed to replace the traditional anode, graphite, which has a relatively low theoretic capacity of 372 mAh g^{-1}.[5,6] Among all anodes, Sn,[7] and Si[8] based anode materials have been widely studied and are on the verge of commercialization. Recently, transition metal oxides have shown high theoretical capacity based on a novel conversion mechanism,[9,10] making them promising candidates for high performance anode materials.[11–15] However, most of these transition metal oxides exhibit poor conductivities, which is lethal for LIB anode application. Iron oxide, Fe_3O_4, is one of the few transition metal oxide materials that possesses both a high theoretical capacity (926 mAh g^{-1}) and a high electronic conductivity.[16] Furthermore, Fe_3O_4 has other advantages, such as natural abundance, low cost and environmental benignity, making such a material an attracting choice for future LIB anodes.[17]

The principal electrochemical process occurring during the charge and discharge cycles of Fe_3O_4 proceeds as follow:[18]

$$Fe_3O_4 + 8\ e^- + 8\ Li^+ \leftrightarrow 3\ Fe^0 + 4\ Li_2O$$

It is reported that lithium binary compound, Li_2O, has been verified to be electrochemically inactive.[9] This property greatly jeopardizes the reversibility of conversion reaction, and also the practical usage of transition metal oxides as LIB anodes. According to the previous reports, the key to improving the reversibility of the conversion reaction is to employ nanosized transition metal particles. Due to the large surface area and thus high activity of the nanoparticles, the Li_2O matrix in which they are embedded can be decomposed when a reverse polarization is applied. Thus, keeping the active phase in the nanosize range is crucial for the reversibility of the conversion reaction, and thus the capacity retention of the anode material.[6,9] Therefore, nanosized iron oxides with different morphologies, such as nanospindles,[16] nanowires,[18] nanoparticles,[19] nanofibers,[20] have been synthesized for LIB anode application. The results from these previous works proved that the reversibility of Fe_3O_4 could be obviously improved when nanosized Fe_3O_4 was adopted.

Another challenge for Fe_3O_4 as a LIB anode material lies in its volume change during lithium ion insertion/removal, which makes iron oxide based electrodes lose structural integrity after several cycles, and consequently leads to breakdown of electrical conduction of the electrode and rapid capacity fading. Such behavior is commonly observed for transition metal oxide anode materials and is one of the major obstacles for this new category of materials to be commercialized. As reported, nanosized anode

[a]Department of Materials Science and Engineering, National University of Singapore, Singapore 117576. E-mail: msexuejm@nus.edu.sg
[b]Department of Mechanical Engineering, National University of Singapore, Singapore 117576

† Electronic supplementary information (ESI) available. See DOI: 10.1039/c2jm15440d

materials can partially solve such a problem because they can better accommodate the strains during Li insertion/removal.[16] Besides, some 3-D structural designs, such as porous and hollow structures,[21–24] have also been proved to be helpful in enhancing the cycling performance of anode materials by providing extra space for volume change during lithium insertion/removal.

In this work, porous hollow Fe_3O_4 beads for LIB anode applications were prepared *via* a facile solvothermal route. The average size of the obtained Fe_3O_4 beads was ~700 nm and each bead was constructed with numerous constituent Fe_3O_4 nanoparticles. The large hollow interior and the pores in between the constituent nanoparticles are able to alleviate the volume change problem during the lithium ion insertion/removal process, thus enhancing the cycling property of such a material in LIB anode application.[22] Carbon coating has been proved to improve the electrochemical performance of nanostructured anode materials due to its high conductivity, good lithium permeability, and flexibility to hold the structure integrity.[25] In this work, a thin layer of carbon was coated onto each Fe_3O_4 bead by using a simple hydrothermal route in order to further improve the capacity retention property. The results demonstrated that the carbon coated Fe_3O_4 beads had improved electrochemical performance compared to bare Fe_3O_4 beads.

Experimental

Materials

Glucose, ethylene glycol (EG), and dodecylamine (DDA) were purchased from Aldrich. Ethanol was purchased from Merck. Sodium hydroxide (NaOH) was purchased from Sigma-Aldrich. Ferric chloride hexahydrate ($FeCl_3 \cdot 6H_2O$) was purchased from Riedel-de Haenwere. All chemicals were used as received.

Preparation of porous hollow magnetite (Fe_3O_4) beads

A 30 mL mix solution containing 2 mmol $FeCl_3 \cdot 6H_2O$, 2 mmol DDA, and 2 mmol NaOH in EG was transferred into a 125 mL Teflon-lined stainless steel autoclave and solvothermally treated in an air-flow electric oven at 200 °C for 4 days. To study the growth mechanism of the beads, the solvothermal processes were stopped at different time intervals (5 h, 9 h, 19 h, 1 d, 2 d, 4 d). After cooling down naturally, the precipitate was collected using a centrifuge and was washed with ethanol. The washed beads were dried at 50 °C for 1 day. An additional carbonization process was carried out if the Fe_3O_4 beads were for electrochemical testing. The black Fe_3O_4 powder was carbonized at 500 °C for 4 h under an inert atmosphere. Subsequently, the Fe_3O_4 beads were washed with ethanol three times and dried at 50 °C for 1 day.

Preparation of carbon coated magnetite (Fe_3O_4/C) beads

25 mg of the as-prepared magnetite beads and 0.25 g glucose were dispersed in 50 mL DI water by ultrasonication. Then the suspension was transferred into a 125 mL Teflon-lined stainless steel autoclave, and hydrothermally treated in an air-flow electric oven at 180 °C for 14 h. After cooling down naturally, the black precipitate was collected by a magnet and washed with ethanol three times. After drying at 50 °C for 1 day, the black precipitate was carbonized at 500 °C for 4 h under an inert atmosphere. Finally, the Fe_3O_4/C beads were washed with ethanol three times and dried at 50 °C for 1 day.

Characterization techniques

The morphologies of samples were examined by scanning electron microscopy (SEM; Zeiss Supra 40 FE), and transmission electron microscopy (TEM) (JEOL 100CX instrument 300 kV). The crystal phases of the samples were characterized by X-ray diffraction analysis (XRD) recorded on a powder diffractometer (Bruker D8 Advanced Diffractometer System) with Cu-Kα (1.5418 A) source. The thermogravimetric analysis (TGA) was performed under an air flow of 100 mL min^{-1} using Du Pont Instruments TGA 2950 from room temperature to 800 °C with a heating rate of 10 °C min^{-1}. X-Ray photoelectron spectroscopy (XPS) measurements were carried out on a Phi Quantera spectrometer using Al Kα X-ray as the excitation source.

Electrochemical measurements

The electrochemical measurements were carried out on Swagelok-type cells using a Neware battery system. To prepare the working electrode, 80 wt% of the active material (Fe_3O_4/C, Fe_3O_4, Fe_2O_3), 10 wt% carbon black and 10 wt% polyvinylidene difluoride (PVDF) dissolved in *N*-methylpyrrolidone (NMP) were mixed to form a slurry. The slurry was pasted on the Cu foil and dried in a vacuum oven for 12 h. The loading of the working electrode is typically in the range of 1–2 mg (~6 mg cm^{-2}). Li foil was used as both the counter and reference electrodes. 1 M $LiPF_6$ in ethylene carbonate and diethyl carbonate (EC/DEC, v/v = 1 : 1) solution was used as the electrolyte. Galvanostatic charge and discharge measurements were carried out in the voltage range between 3.0 and 0.05 V at current densities of 100 and 500 mA g^{-1}.

Results and discussion

Fig. 1A presented the SEM image of the Fe_3O_4 beads obtained at 200 °C for 4 days *via* a solvothermal route. The as-prepared beads were spherical in morphology and had good monodispersity. The bar chart shown in the inset of Fig. 1A indicated that the average size of these beads was around 700 nm. From the SEM image with the higher magnification shown in Fig. 1B, the surface morphology of the Fe_3O_4 beads was clearly revealed. Each Fe_3O_4 bead was constructed with numerous Fe_3O_4 nanoparticles. More importantly, these constituent nanoparticles were not densely packed. Lots of void space could be found in between them, making the whole Fe_3O_4 bead a highly porous structure. Fig. 1C showed the TEM image of the as-obtained Fe_3O_4 beads at low magnification. Through the clear variation in contrast, the porous and hollow nature of the beads was further confirmed. Moreover, most pores were channel-like, connecting the central hollow interior and the outside space. The TEM image of a single Fe_3O_4 bead was shown in Fig. 1D. To achieve more detailed crystallographic information of the constituent nanoparticles, a high resolution TEM image was taken at the conjunction of three constituent Fe_3O_4 nanoparticles (boxed region in Fig. 1D), which was shown in Fig. 1E. Interestingly, all these three nanoparticles shared one common crystallographic

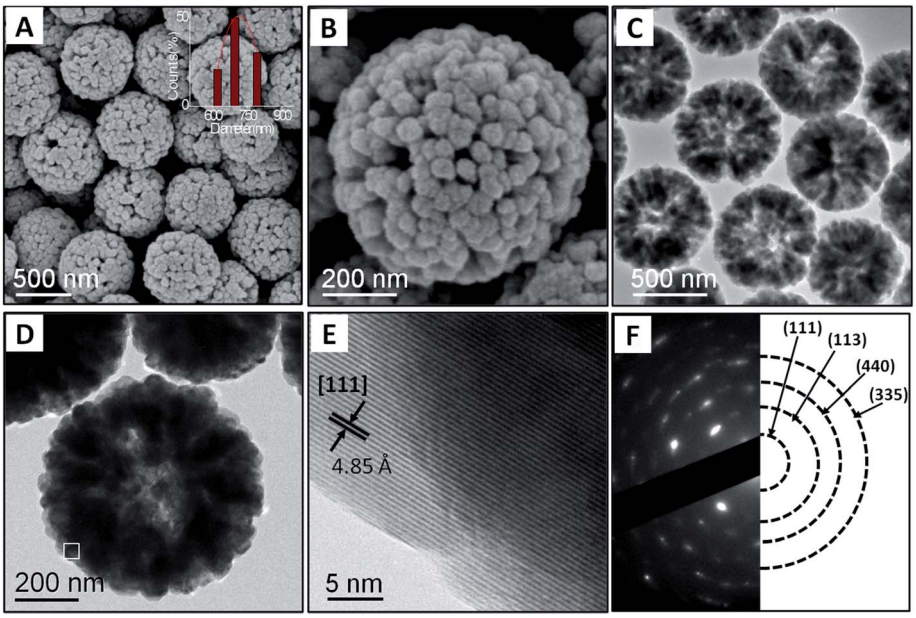

Fig. 1 (A, B) SEM images of the as-prepared Fe_3O_4 beads. Inset of A: the diameter distribution of the as-prepared Fe_3O_4 beads. (C, D) TEM images of the as-prepared Fe_3O_4 beads. (E) HRTEM of the highlighted region in D. (F) SAED pattern of the as-prepared Fe_3O_4 beads.

orientation. The lattice fringe calculated from the HRTEM image was 4.85 Å, fitting well with the (111) planes of a cubic Fe_3O_4 structure. The common crystallographic alignment of the Fe_3O_4 nanoparticles suggested that oriented assembly occurred in the synthesized Fe_3O_4 beads.[26,27] The solvent EG used in the synthesis process played a crucial role in such oriented assembly. Compared with fast aggregation growth which occurred in an aqueous environment, the Fe_3O_4 nanoparticles formed in EG solvent aggregated slower due to the greater solvent viscosity.[28] During the formation process of Fe_3O_4 beads, the newly formed Fe_3O_4 nanoparticles in solution slowly attached on the surface of the pre-formed Fe_3O_4 aggregates.[29] In an effort to reduce the overall energy of the system, the approaching Fe_3O_4 nanoparticles rotated so that adjacent primary Fe_3O_4 nanoparticles self-organized into a common crystallographic orientation, and finally fused together to form the secondary Fe_3O_4 nanoparticles. The SAED pattern shown in Fig. 1F showed the diffraction result of a single Fe_3O_4 bead. Instead of commonly observed diffraction rings for normal nanoparticle aggregates, a dot-like pattern was observed, confirming the occurrence of oriented attachment. Besides, the SAED dot pattern revealed the crystalline nature of the as-synthesized Fe_3O_4 beads, which fit the cubic magnetite structure (JCPDS 65-3107) well.

In order to investigate the formation mechanisms of the obtained porous hollow Fe_3O_4 beads, products at different solvothermal reaction intervals were collected and their morphologies and crystal structures were characterized using SEM and XRD, respectively. The corresponding results were shown in Fig. 2. All SEM images were observed at the same magnification so that the growth process of the Fe_3O_4 beads could be clearly observed. As shown in Fig. 2A, spindle shaped particles with a length around 100 nm were obtained when the solvothermal reaction time was 5 h. The corresponding XRD pattern shown in Fig. 2G indicated that these spindle particles belonged to $Fe_2O_3 \cdot H_2O$ (JCPDS 13-0092) instead of Fe_3O_4. This was due to the fact that most of the Fe^{3+} precursor was not yet reduced by EG at the early stage of the synthesis process. When the reaction was extended to 9 h (Fig. 2B), a small amount of spherical aggregates was formed, but there was no obvious change in the XRD pattern as compared to the 5 h sample. By increasing the reaction time to 19 h, as indicated by Fig. 2C, most of the produced precipitates consisted of spherical aggregates, which belonged to Fe_3O_4 phase suggested by the XRD (Fig. 2G). Upon the reaction for one day, the produced precipitates were purely Fe_3O_4 spherical aggregates and there were no Fe_2O_3 spindle nanoparticles left (Fig. 2D). When the reaction time was extended from 1 day to 2 days (Fig. 2E), the size of the aggregates was significantly increased from 250 nm to 700 nm. The size of the constituent Fe_3O_4 nanoparticles was also increased. The inset of Fig. 2E showed a broken spherical aggregate by the reaction time of 2 days. It could be seen that the aggregate was still solid in the interior. It was also worthy to note that the constituent Fe_3O_4 nanoparticles at the outer surface of the aggregate were rod-shaped, which were formed by the oriented attachment of primary Fe_3O_4 nanoparticles as discussed previously. These rod-shaped Fe_3O_4 nanoparticles were larger in size compared to the central primary Fe_3O_4 nanoparticles. When the reaction was finally extended to 4 days, porous Fe_3O_4 beads were formed, as shown in Fig. 2F. Through the SEM image of a broken bead shown in the inset of Fig. 2F, the hollow interior of the bead was further revealed.[30,31] Numerous rod-shaped Fe_3O_4 nanoparticles were packed together, constructing the shell of the hollow bead. The formation of the obtained hollow porous Fe_3O_4 beads was a result of a process known as Ostwald ripening.[32,33] As shown in the inset of Fig. 2E, there was a size difference between the outer and inner particles of the aggregates. The larger particles at the outer surface were able to grow at the expense of the inner particles, leading to an evacuation process based on inside-out ripening, resulting in a hollow interior of the beads.[34–38] Besides, some outer Fe_3O_4 nanoparticles, which were relatively small in

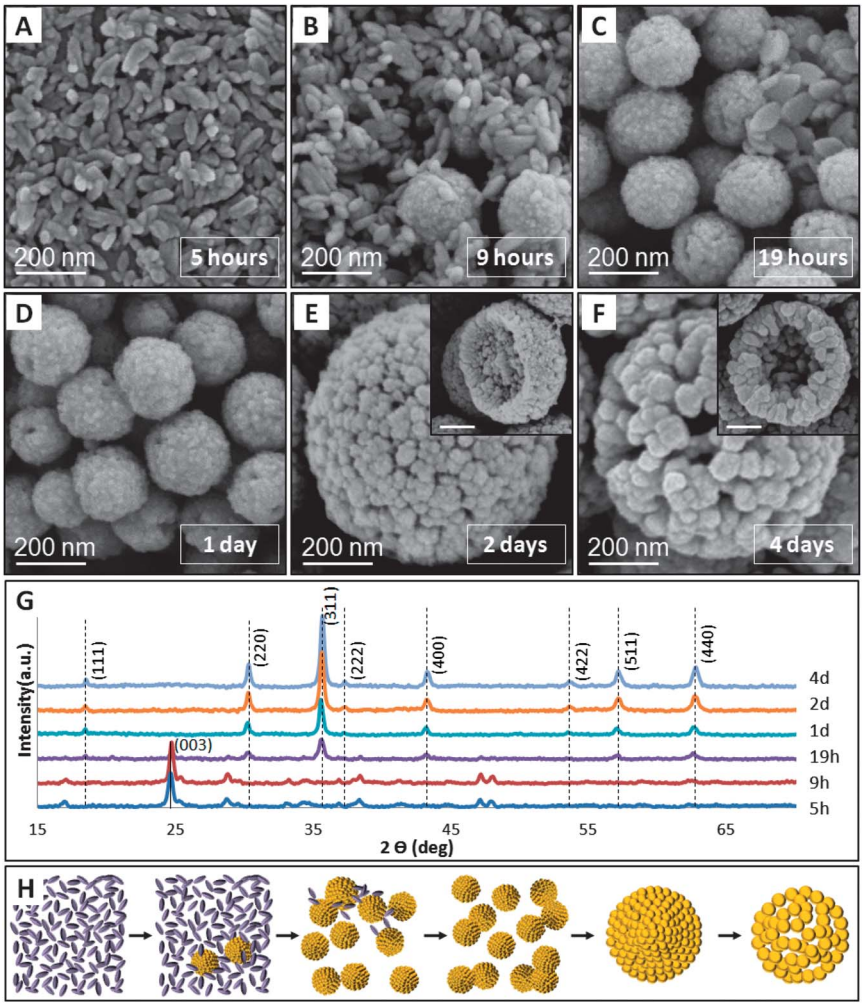

Fig. 2 SEM images of the products collected at different intervals: (A) 5 h, (B) 9 h, (C) 19 h, (D) 1 day, (E and its inset) 2 days, and (F and its inset) 4 days. All scale bars (including the ones in the insets) are 200 nm. (G) Corresponding XRD patterns of the products collected at different intervals. Dash lines correspond to the standard peak positions of the cubic magnetite structure. The solid line shows the characteristic peak of the $Fe_2O_3 \cdot H_2O$ phase. (H) Schematic representation of the formation of hollow porous Fe_3O_4 beads. Purple and yellow particles correspond to the Fe_2O_3 and Fe_3O_4 phase, respectively.

size, were also consumed at the expense of the growth of the larger ones, leading to the formation of a porous structure. Fig. S1 in the ESI demonstrated the magnetic response of the solvothermal products at different reaction intervals.† When the reaction time was beyond 19 h, the products could be attracted by a magnet, suggesting the successful formation of the Fe_3O_4 structures.

Fig. 2H summarized the key steps for the formation of the porous hollow Fe_3O_4 beads in the employed solvothermal process. As a first step, raw $FeCl_3 \cdot 6H_2O$ was hydrolyzed into $Fe_2O_3 \cdot H_2O$ (spindle-like nanoparticles) under solvothermal conditions with the assistance of NaOH. This was followed with a reduction process of $Fe_2O_3 \cdot H_2O$ by EG, leading to the formation of Fe_3O_4 nanoparticles. The aggregation of the Fe_3O_4 nanoparticles occurred due to the combining effect of surfactant DDA and water which was introduced with the raw materials.[28] The well defined Fe_3O_4 spherical aggregates could be formed upon two days of reaction. By further extending the reaction time, the solid Fe_3O_4 aggregates evolved into porous and hollow structures due to the Ostwald ripening process under the solvothermal condition.

Carbon coating has been reported extensively as a modification technique for anode materials to enhance the capacity retention property.[18,25,39] Firstly, with a uniform carbon coating, the conductivity of an anode material can be greatly enhanced. Secondly, the carbon coating layer is able to act as a barrier to protect the inner active materials.[19] Besides, the carbon layer is flexible so that it can hold the structure integrity against the huge volume change of active materials (Fe_3O_4) during the lithium ion insertion/removal process.[25] In this work, the obtained Fe_3O_4 beads were further coated with carbon by using glucose as the carbon source *via* a hydrothermal route. Under the high temperature and high pressure condition in the autoclave, glucose molecules underwent a polymerization, condensation and aromatization process, forming smooth carbon-rich solid layers on the surface of the Fe_3O_4 beads.[40,41] After heat treatment in an inert atmosphere, the oxygen functional groups contained in the carbon-rich layer were removed, leaving a carbon coating

layer. Fig. 3A shows the SEM image of the carbon coated Fe_3O_4 (Fe_3O_4/C) beads, which showed similar morphologies to beads without carbon coating. The inset of Fig. 3A showed a single Fe_3O_4/C bead with a higher magnification. Compared to the bare Fe_3O_4 bead, the surface of the Fe_3O_4/C bead was much smoother. Besides, small holes in between the constituent Fe_3O_4 nanoparticles were covered. Fig. 3B showed the TEM image of a single carbon coated Fe_3O_4 bead. Through the clear difference in contrast, the hollow nature of the Fe_3O_4 beads was well preserved after carbon coating. The inset of Fig. 3B showed a magnified TEM image of the highlighted region of Fig. 3B, providing a better observation of the surface morphology of such Fe_3O_4/C beads. Compared with the bare Fe_3O_4 bead surface shown in Fig. S2 of the ESI,† a thin and continuous carbon layer could be clearly observed (indicated by an arrow). The carbon content of the Fe_3O_4/C beads was further verified using TGA measurement. As shown in Fig. 3C, a small overall decline in total mass (~3%) was observed for the bare Fe_3O_4 beads, which was caused by the removal of the residual water and surfactants. Besides, a small hump was observed between 300 and 500 °C, which was ascribed to the oxidation of Fe_3O_4 to Fe_2O_3. For the TGA curve of the Fe_3O_4/C beads, an obvious weight loss of ~18% occurred at around 300 °C. Another 5% weight loss was observed when the sample was further heated to 770 °C. By comparing the TGA curve of the Fe_3O_4/C beads with that of the bare ones, the carbon content of the Fe_3O_4/C beads was determined to be around 20%. To determine the surface chemical compositions before and after carbon coating, XPS measurements were carried out for bare Fe_3O_4 and Fe_3O_4/C beads. As shown in Fig. S3 of the ESI,† after a hydrothermal step with glucose followed by a calcination process under an inert atmosphere, the intensity of the C 1s spectrum of the Fe_3O_4/C beads (Fig. S3A†) increased tremendously compared to that of bare Fe_3O_4 beads, while the intensities of the O 1s (Fig. S3B†) and Fe 2p (Fig. S3C†) spectra decreased sharply after coating, indicating that the Fe_3O_4 beads' surfaces have been covered by a layer of carbon. The relative atomic percentages shown in Fig. S3D also confirmed the successful coating of carbon.†

The electrochemical performance of the as-obtained Fe_3O_4/C, Fe_3O_4 and α-Fe_2O_3 beads (α-Fe_2O_3 beads were obtained by oxidizing the Fe_3O_4 beads at 450 °C. The corresponding SEM and XRD for the α-Fe_2O_3 beads were presented in Fig. S4 of the ESI) with respect to Li insertion/removal were investigated. Fig. 4A showed the discharge/charge profiles for Fe_3O_4/C composite beads at a current density of 100 mA g^{-1}. A potential plateau at around 0.8 V *versus* Li^+/Li was observed in the first discharge curve, which was similar to literature descriptions for Fe_3O_4 based anodes.[16,42] Form the theoretical capacity of Fe_3O_4

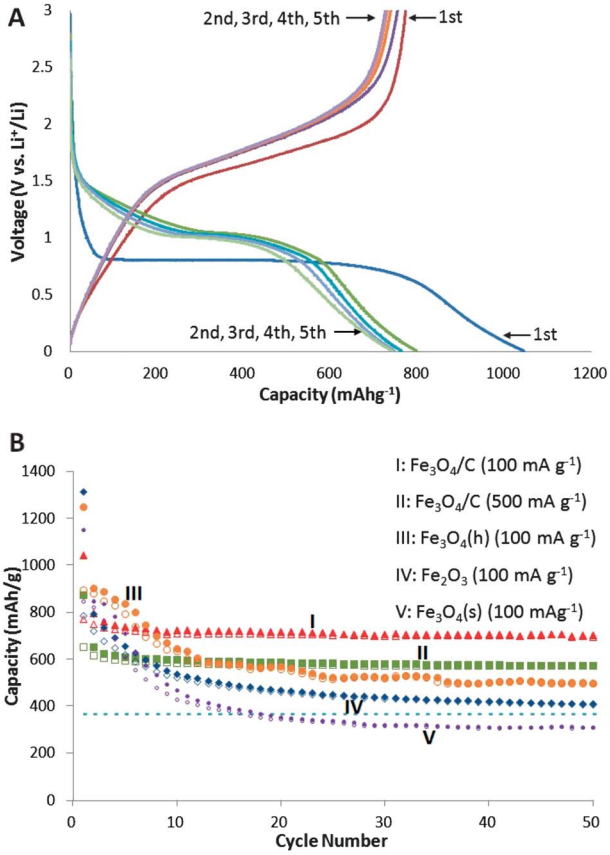

Fig. 4 (A) The discharge/charge profiles of the Fe_3O_4/C composite beads at a current density of 100 mA g^{-1}. (B) Discharge and charge capacity (lithium storage) *vs.* cycle number between 3 V and 5 mV, (I) Fe_3O_4/C composite beads with a current density of 100 mA g^{-1} (solid and hollow triangles), (II) Fe_3O_4/C composite beads with a current density of 500 mA g^{-1} (solid and hollow squares), (III) hollow Fe_3O_4 beads with a current density of 100 mA g^{-1} (solid and hollow spheres), (IV) bare Fe_2O_3 beads with a current density of 100 mA g^{-1} (solid and hollow diamonds), (V) bare solid Fe_3O_4 beads with a current density of 100 mA g^{-1} (solid and hollow dots). The dash line is the theoretical capacity of graphite.

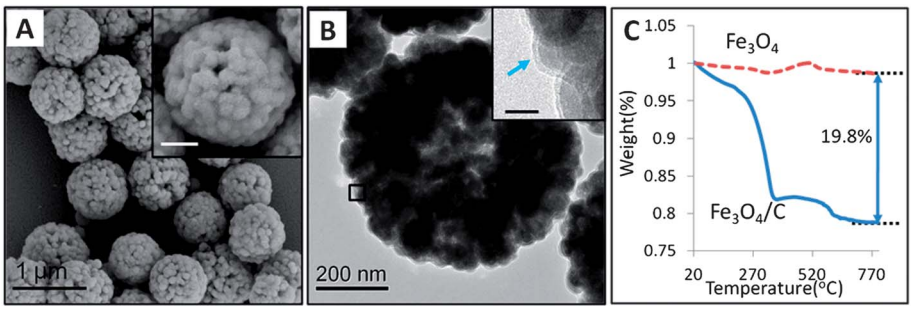

Fig. 3 (A and inset) SEM images of Fe_3O_4/C beads. Scale bar of inset: 200 nm. (B) TEM image of a Fe_3O_4/C bead. Inset: magnified surface morphology of the Fe_3O_4/C bead. Scale bar of inset: 20 nm. (C) TGA curves of the as-obtained Fe_3O_4 and Fe_3O_4/C beads.

and the carbon content percentage obtained previously, the theoretical specific capacity of the as-obtained Fe_3O_4/C composite beads could be calculated to be around 816 mAh g^{-1}. As indicated in the discharge/charge profiles (Fig. 4A), the first specific charge capacity of Fe_3O_4/C was 772 mAh g^{-1}, which was around 94% of its theoretical capacity. The irreversible capacity in the first cycle can be attributed to the decomposition of electrolyte and formation of solid electrolyte interface. The cycling performances of the Fe_3O_4/C composite beads were shown in Fig. 4B (I). With a current rate of 100 mA g^{-1}, after a small initial decay, the capacity of the Fe_3O_4/C beads stabilized around 700 mAh g^{-1}, and delivered a capacity of 698.8 mAh g^{-1} based on the mass of both Fe_3O_4 and carbon coating, or 873.5 mAh g^{-1} without consideration of the carbon coating mass at the 50th cycle. Such a high capacity was attributed to the combining effect of the high theoretical capacity of the Fe_3O_4 material, nanosized constituent Fe_3O_4 particles, specially designed hollow and porous structure, and the carbon coating. The Fe_3O_4/C composite beads were also tested with a higher current density (500 mAh g^{-1}). As shown in Fig. 4B (II), a lower but stable capacity curve was obtained, which delivered a capacity of 573.1 mAh g^{-1} (based on the total mass of Fe_3O_4 and carbon coating) or 716.4 mAh g^{-1} (based only on the mass of Fe_3O_4) at the 50th cycle. In order to demonstrate the effect of carbon coating, the electrochemical performance of the hollow Fe_3O_4 beads was tested as a comparison. As shown in Fig. 4B (III), without the carbon coating layer, the capacity of the hollow Fe_3O_4 beads experienced a fast initial decay and finally stabilized around 500 mAh g^{-1} after 50 cycles. As suggested by such electrochemical testing results, with the carbon coating layer, the capacity retention property of the Fe_3O_4 material can be greatly improved for about 200 mAh g^{-1} after 50 cycles, demonstrating the crucial effect of carbon coating in enhancing the cycling performance of anode materials.[43,44] Fig. S5 provided an insight behind these numerical data in terms of the morphological changes of bare Fe_3O_4 and Fe_3O_4/C beads after 50 cycles of charging/discharging.† A small number of broken beads can be found in the bare Fe_3O_4 sample after 50 cycles of electrochemical testing. Fig. S5A showed the morphology of a typical broken Fe_3O_4 bead.† However, almost all Fe_3O_4/C beads preserved intact structures after 50 times of cycling (Fig. S5B†), demonstrating the crucial effect of carbon coating in holding the structure integrity of these hollow and porous Fe_3O_4 beads. The cycling performance of the hollow Fe_2O_3 beads was also tested as a comparison. As shown in Fig. 4B (IV), the capacity of the hollow Fe_2O_3 beads dropped even faster than that of hollow Fe_3O_4 beads and delivered a capacity of 409 mAh g^{-1} at the 50th cycle. This was mainly caused by its lower conductivity as compared to Fe_3O_4. In order to investigate the effect of the hollow structure on the electrochemical behavior, the cycling performance of solid Fe_3O_4 beads obtained after 2 days solvothermal process (Fig. 2E) was also tested at a current density of 100 mA g^{-1}. As shown in Fig. 4B (V), the fastest capacity fading among all samples was observed with a reversible capacity at the 50th cycle of 311 mAh g^{-1}, demonstrating the important effect of the hollow interior on enhancing the capacity retention property of the Fe_3O_4 beads by mitigating the volume change during the lithium insertion/removal process.

Conclusions

In summary, porous hollow Fe_3O_4 beads for lithium ion battery anodes were synthesized *via* a facile solvothermal route. The growth process for the porous hollow beads was carefully monitored and the synthesis mechanism based on oriented assembly and Ostwald ripening was proposed. The large void space in between the constituent Fe_3O_4 nanoparticles and hollow interior of the as-obtained beads were desirable to mitigate the volume change problem during the Li ion insertion/removal process. A layer of carbon coating was incorporated on the surface of each Fe_3O_4 bead to enhance its conductivity and structure integrity. Compared with the bare Fe_3O_4 beads, carbon coated Fe_3O_4 (Fe_3O_4/C) composite beads delivered an enhanced specific capacity around 700 mAh g^{-1} at a current rate of 100 mA g^{-1} after 50 cycles, showing their promising application for high performance lithium ion batteries.

Acknowledgements

The authors thank the financial support provided by Singapore MOE Tier 1 grant R-284-000-088-112.

References

1 M. Armand and J. M. Tarascon, *Nature*, 2008, **451**, 652–657.
2 K. Kang, Y. S. Meng, J. Breger, C. P. Grey and G. Ceder, *Science*, 2006, **311**, 977–980.
3 P. G. Bruce, B. Scrosati and J. M. Tarascon, *Angew. Chem., Int. Ed.*, 2008, **47**, 2930–2946.
4 J. M. Tarascon and M. Armand, *Nature*, 2001, **414**, 359.
5 J. B. Goodenough and Y. Kim, *Chem. Mater.*, 2010, **22**, 587–603.
6 J. Liu and D. Xue, *Nanoscale Res. Lett.*, 2010, **5**, 1525–1534.
7 G. Derrien, J. Hassoun, S. Panero and B. Scrosati, *Adv. Mater.*, 2007, **19**, 2336–2340.
8 F. F. Cao, J. W. Deng, S. Xin, H. X. Ji, O. G. Schmidt, L. J. Wan and Y. G. Guo, *Adv. Mater.*, 2011, **23**, 4415–4420.
9 P. Poizot, S. Laruelle, S. Grugeon, L. Dupont and J. M. Tarascon, *Nature*, 2000, **407**, 496–499.
10 J. Cabana, L. Monconduit, D. Larcher and M. R. Palacin, *Adv. Mater.*, 2010, **22**, E170–E192.
11 H. W. Shim, Y. H. Jin, S. D. Seo, S. H. Lee and D. W. Kim, *ACS Nano*, 2011, **5**, 443–449.
12 S. Grugeon, S. Laruelle, R. Herrera-Urbina, L. Dupont, P. Poizot and J. M. Tarascon, *J. Electrochem. Soc.*, 2001, **148**, A285–A292.
13 P. L. Taberna, S. Mitra, P. Poizot, P. Simon and J. M. Tarascon, *Nat. Mater.*, 2006, **5**, 567–573.
14 J. Liu, H. Xia, D. Xue and L. Lu, *J. Am. Chem. Soc.*, 2009, **131**, 12086–12087.
15 J. Liu, Y. Zhou, J. Wang, Y. Pan and D. Xue, *Chem. Commun.*, 2011, **47**, 10380–10382.
16 W. M. Zhang, X. L. Wu, J. S. Hu, Y. G. Guo and L. J. Wan, *Adv. Funct. Mater.*, 2008, **18**, 3941–3946.
17 Z. M. Cui, L. Y. Jiang, W. G. Song and Y. G. Guo, *Chem. Mater.*, 2009, **21**, 1162–1166.
18 T. Muraliganth, A. V. Murugan and A. Manthiram, *Chem. Commun.*, 2009, 7360–7362.
19 Y. Piao, H. S. Kim, Y. E. Sung and T. Hyeon, *Chem. Commun.*, 2010, **46**, 118–120.
20 L. Wang, Y. Yu, P. C. Chen, D. W. Zhang and C. H. Chen, *J. Power Sources*, 2008, **183**, 717–723.
21 R. Demir-Cakan, Y. S. Hu, M. Antonietti, J. Maier and M. M. Titirici, *Chem. Mater.*, 2008, **20**, 1227–1229.
22 D. Deng and J. Y. Lee, *Chem. Mater.*, 2008, **20**, 1841–1846.
23 F. Liu and D. Xue, *Nanosci. Nanotechnol. Lett.*, 2011, **3**, 389–393.
24 J. Liu, H. Xia, L. Lu and D. Xue, *J. Mater. Chem.*, 2010, **20**, 1506–1510.
25 Y. Chen, Q. Z. Huang, J. Wang, Q. Wang and J. M. Xue, *J. Mater. Chem.*, 2011, **21**, 17448–17453.

26 A. P. Alivisatos, *Science*, 2000, **289**, 736–737.
27 A. Narayanaswamy, H. Xu, N. Pradhan and X. Peng, *Angew. Chem., Int. Ed.*, 2006, **45**, 5361–5364.
28 D. Yu, X. Sun, J. Zou, Z. Wang, F. Wang and K. Tang, *J. Phys. Chem. B*, 2006, **110**, 21667–21671.
29 R. Liu, Y. Zhao, R. Huang, Y. Zhao and H. Zhou, *Eur. J. Inorg. Chem.*, 2010, 4499–4505.
30 C. Luo and D. Xue, *Langmuir*, 2006, **22**, 9914–9918.
31 J. Wu and D. Xue, *Nanosci. Nanotechnol. Lett.*, 2011, **3**, 400–406.
32 X. W. Lou, L. A. Archer and Z. Yang, *Adv. Mater.*, 2008, **20**, 3987–4019.
33 H. G. Yang and J. C. Zeng, *J. Phys. Chem. B*, 2004, **108**, 3492–3495.
34 X. M. Yin, C. C. Li, M. Zhang, Q. Y. Hao, S. Liu, L. B. Chen and T. H. Wang, *J. Phys. Chem. C*, 2010, **114**, 8084–8088.
35 H. G. Yang and H. C. Zeng, *Angew. Chem., Int. Ed.*, 2004, **43**, 5930–5933.
36 S. Liu, R. Xing, F. Lu, R. K. Rana and J. J. Zhu, *J. Phys. Chem. C*, 2009, **113**, 21042–21047.
37 J. Liu, F. Liu, K. Gao, J. Wu and D. Xue, *J. Mater. Chem.*, 2009, **19**, 6073–6084.
38 J. Liu and D. Xue, *Adv. Mater.*, 2008, **20**, 2622–2627.
39 J. Liu, Y. Li, H. Fan, Z. Zhu, J. Jiang, R. Ding, Y. Hu and X. Huang, *Chem. Mater.*, 2010, **22**, 212–217.
40 M. Sevilla and A. B. Fuertes, *Chem.–Eur. J.*, 2009, **15**, 4195–4203.
41 X. W. Lou, J. S. Chen, P. Chen and L. A. Archer, *Chem. Mater.*, 2009, **21**, 2868–2874.
42 G. Zhou, D. W. Wang, F. Li, L. Zhang, N. Li, Z. S. Wu, L. Wen, G. Q. Lu and H. M. Cheng, *Chem. Mater.*, 2010, **22**, 5306–5313.
43 W. M. Zhang, J. S. Hu, Y. G. Guo, S. F. Zheng, L. S. Zhong, W. G. Song and L. J. Wan, *Adv. Mater.*, 2008, **20**, 1160–1165.
44 G. Cui, Y. S. Hu, L. Zhi, D. Wu, I. Lieberwirth, J. Maier and K. Mullen, *Small*, 2007, **3**, 2066–2069.

